Direct momentum imaging of charge transfer following site-selective ionization

Felix Allum,[1,2,3,*] Yoshiaki Kumagai,[4] Kiyonobu Nagaya,[5] James Harries,[6] Hiroshi Iwayama,[7,8] Mathew Britton,[2] Philip H. Bucksbaum,[2] Michael Burt,[1] Mark Brouard,[1] Briony Downes-Ward,[9] Taran Driver,[3] David Heathcote,[1] Paul Hockett,[10] Andrew J. Howard,[2] Jason W. L. Lee,[11] Yusong Liu,[2] Edwin Kukk,[12] Joseph W. McManus,[1] Dennis Milsesevic,[1] Akinobu Niozu,[13] Johannes Niskanen,[12] Andrew J. Orr-Ewing,[14] Shigeki Owada,[15,16] Patrick A. Robertson,[1] Artem Rudenko,[17] Kiyoshi Ueda,[18] James Unwin,[1] Claire Vallance,[1] Tiffany Walmsley,[1] Russell S. Minns,[9] Daniel Rolles,[17] Michael N. R. Ashfold,[14] and Ruaridh Forbes[3,†]

[1] *Chemistry Research Laboratory, Department of Chemistry, University of Oxford, Oxford OX1 3TA, UK*
[2] *PULSE Institute, SLAC National Accelerator Laboratory, 2575 Sand Hill Road, Menlo Park, CA 94025, USA*
[3] *Linac Coherent Light Source, SLAC National Accelerator Laboratory, 2575 Sand Hill Road, Menlo Park, CA 94025, USA*
[4] *Department of Applied Physics, Tokyo University of Agriculture and Technology, Tokyo, Japan*
[5] *Department of Physics, Kyoto University, Kyoto 606-8502, Japan*
[6] *QST, SPring-8, Kouto 1-1-1, Sayo, Hyogo, Japan*
[7] *Institute for Molecular Science, Okazaki 444-8585, Japan*
[8] *Sokendai (The Graduate University for Advanced Studies), Okazaki 444-8585, Japan*
[9] *School of Chemistry, University of Southampton, Highfield, Southampton SO17 1BJ, UK*
[10] *National Research Council of Canada, 100 Sussex Dr. Ottawa, ON K1A 0R6, Canada*
[11] *Deutsches Elektronen-Synchrotron DESY, Hamburg, Germany*
[12] *Department of Physics and Astronomy, University of Turku, FI-20014 Turku, Finland*
[13] *Graduate School of Advanced Science and Engineering, Hiroshima University, Higashi-Hiroshima 739-8526, Japan*
[14] *School of Chemistry, University of Bristol, Cantock's Close, Bristol BS8 1TS, UK*
[15] *RIKEN SPring-8 Center, Sayo, Hyogo, 679-5148, Japan*
[16] *Japan Synchrotron Radiation Research Institute, Hyogo, Japan*
[17] *J.R. Macdonald Laboratory, Department of Physics, Kansas State University, Manhattan, Kansas 66506, USA*
[18] *Department of Chemistry, Tohoku University, Sendai 980-8578, Japan*

(Dated: September 26, 2023)

We study ultrafast charge rearrangement in dissociating 2-iodopropane (2-C_3H_7I) using site-selective core-ionization at the iodine atom. Clear signatures of electron transfer between the neutral propyl fragment and multiply charged iodine ions are observed in the recorded delay-dependent ion momentum distributions. The detected charge transfer pathway is only favorable within a small (few angstrom), charge-state-dependent spatial window located at C-I distances longer than that of the neutral ground-state molecule. These results offer new insights into the physics underpinning charge transfer in isolated molecules and pave the way for a new class of time-resolved studies.

Charge rearrangement within and between molecules is of fundamental importance throughout physics [1–5], chemistry [6–8] and biology [9, 10]. Detailed studies of isolated gas-phase molecules offer a powerful route to probing the mechanistic basis of such phenomena. Recent advances in free-electron lasers (FELs) have yielded sources of intense, coherent pulses of X-ray and extreme ultraviolet (XUV) light [11–13], capable of targeting individual atomic orbitals within molecules [14–18]. Multiple ionization at a specific atomic site creates a highly localized charge from which charge transfer (CT) may proceed. This is closely related to collisional CT between multiply charged ions and neutrals which is of astrophysical significance, for instance as the source of electronically excited ions that can cause X-ray emissions from comets and solar winds [2–5].

In pioneering work, Erk *et al.* dissociatively ionized CH_3I using a strong near-infrared laser field, prior to ionizing the departing iodine atom with a FEL-based X-ray probe pulse [1]. Observed low-momentum I^{n+} ions were assigned to site-selective ionization of the departing iodine fragment. This feature's appearance was delayed from the time of the pump excitation, and this delay increased for higher iodine charge states. The n-dependent, delayed onset of this feature is a consequence of CT: when the iodine is multiply ionized to $I^{(n+1)+}$ at short pump-probe delays, positive charge can transfer to the recoiling CH_3 fragment. Both fragments are now positively charged and Coulombically repel, yielding higher-momentum I^{n+} ions and consequently quenching low-momentum $I^{(n+1)+}$ ion production. For higher iodine charge states, this CT can occur over greater internuclear separations

* fallum@stanford.edu
† ruforbes@stanford.edu

(thus, longer pump-probe delays), as qualitatively predicted by the classical over-the-barrier model [1, 19, 20]. In short, the over-the-barrier model considers the Coulombic potential between the two sites for a range of internuclear separations. As internuclear distance increases, the Coulombic barrier between the two sites increases, leading to the concept of a charge-state-dependent 'critical distance', at which this barrier is equal to the binding energy of the transferring valence electron. Beyond this distance, the electron transfer is considered forbidden. A more detailed account of the over-the-barrier model is given in Appendix E. Follow-up work has examined CT in a series of halogenated molecules using, for the pump step, either multiphoton ionization or single-photon UV-induced dissociation analyzing this delayed low-momentum ion feature [18, 21–24].

In principle, delay-dependent momentum distributions of the repelling ions produced from CT and subsequent Coulomb repulsion are richly informative, encoding information about the geometry at the point of CT and the number of electrons transferred. However, such signal could not be isolated in previous experiments, due to its overlap with signal from probe-only Coulomb explosion of unpumped molecules [21, 23, 24], or from Coulombically repelling species produced by probing a dissociative ionization [1, 18]. Here, we present results from an experimental investigation into CT within dissociating 2-iodopropane molecules, in which the Coulombically repelling fragments produced by single charge transfer are isolated and analyzed in detail. We identify narrow regions of interfragment separation at which this CT channel occurs, map how this varies with iodine charge state and observe evidence for nuclear motion after site-selective ionization yet prior to CT.

Molecules of 2-iodopropane were photoexcited by a ∼100-fs ultraviolet (UV) laser pulse with a 267-nm central wavelength, prior to ionization by a ∼30-fs 95-eV XUV laser pulse produced by the SACLA soft X-ray FEL [25]. UV photoabsorption initiates prompt photodissociation of 2-iodopropane by populating repulsive potential energy surfaces (PESs) following a $n_I \rightarrow \sigma_{C-I}^*$ transition [26, 27].

Atomic Xe and molecular C_3H_8 (logical analogues of atomic I and C_3H_7) have photoabsorption cross-sections of ∼25 Mb [28] and ∼1.3 Mb [29], respectively, at 95 eV. Ionization is thus expected to occur selectively at the iodine atom, with the initial I 4d ionization depositing either two or three total positive charges on the molecule (in an approximately 2:1 ratio [28]) following Auger-Meitner (AM) decay(s) [50]. The observation of I^{n+} ions with n as high as 6 in the present study therefore indicates that multiple photoabsorptions can occur. Following site-selective ionization, positive charge may either remain localized at the iodine, or transfer to the neutral alkyl fragment and induce Coulombic repulsion and an increase in the iodine ion momentum. These processes are shown schematically in Fig. 1(a).

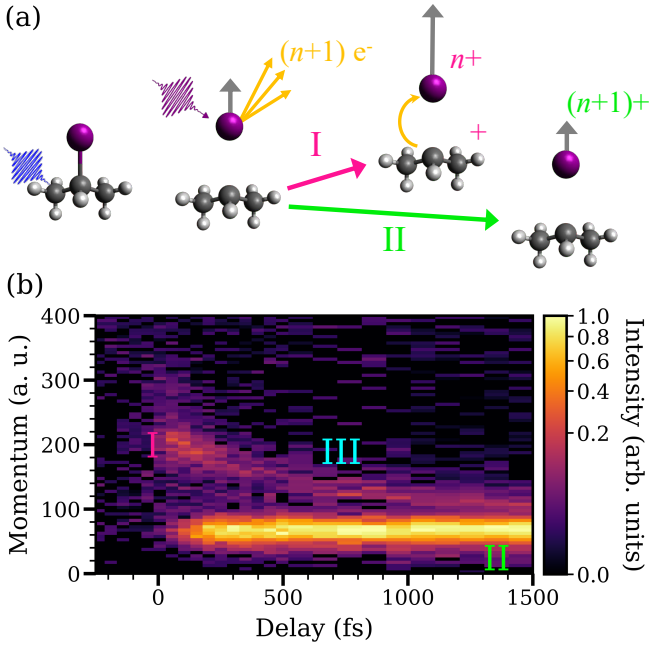

FIG. 1. (a) Experimental schematic, showing UV-induced neutral C-I bond fission in 2-iodopropane followed by site-selective multiple ionization at the iodine atom to its $(n+1)+$ charge state and two possible outcomes, in which either an electron is transferred between fragments (pathway I) or charge remains localized at the iodine (pathway II). The momentum of the iodine ion is indicated by the gray arrow. (b) Momentum distribution in atomic units (a.u.) of the I^{4+} ion as a function of delay between the UV pump and XUV probe lasers. Positive (negative) delays correspond to the UV pulse arriving first (second). In this plot and throughout the manuscript, XUV-only contributions have been removed by subtracting scaled averaged data before time-zero. Data prior to subtraction are shown in Figure 4 in Appendix B. Three distinct pump-probe features are observed, labelled I-III (see text).

The three-dimensional momenta of ionic fragments were recorded in a velocity-map imaging [30] spectrometer [31] as a function of the jitter-corrected pump-probe delay [32]. The experimental setup is described in detail in Appendix A.

Figure 1(b) shows the recorded delay-dependent I^{4+} momentum distribution. Three pump-probe features are recognized. Promptly after time-zero, a transient enhancement is observed in the higher-momentum region labelled 'I'. The strongest feature, 'II', exhibits a constant low momentum, appears shortly after time-zero and persists to long pump-probe delays. A weaker feature, 'III', appears after time-zero and exhibits a momentum which decreases with increasing delay. Analogous features are observed for all multiply charged $I^{(2-6)+}$ ions observed (although I^{3+} is excluded from most of the analysis due to its overlapping mass-to-charge ratio with $C_3H_7^+$), as shown in Fig. 5 in Appendix B.

Channels I to III may be assigned to the following

processes following UV photoexcitation:

I: Site-selective XUV ionization at the iodine atom to produce $I^{(n+1)+}$ ions, followed by CT to the neutral propyl cofragment to yield I^{n+} and $C_3H_7^+$ (and potentially any smaller fragments derived therefrom) at the earliest stages of C-I bond extension, which Coulombically repel.

II: Site-selective XUV ionization at the departing iodine atom without subsequent CT.

III: XUV ionization of both the separating iodine and propyl fragments, producing a multiply charged iodine ion and a singly charged alkyl cofragment.

Note, the images obtained in this study are for iodine ions in a specific final charge state. An I^{n+} image necessarily reports on parent molecules initially promoted to the $(n+1)+$ charge state in the case of Channel I, but on I atoms promoted to just the $n+$ charge state in the case of Channels II and III.

The momentum and angular distributions of the Channel II products agree well with literature measurements of the neutral UV photodissociation of 2-iodopropane [26], as the XUV ionization process does not substantially alter the momentum of the recoiling iodine fragment. The significantly greater momenta of Channels I and III arise from Coulomb repulsion against a singly charged alkyl fragment, which decreases for longer pump-probe delays (greater internuclear separations) [33, 34]. As shown in Fig 6 of Appendix C, Channels I and II exhibit very similar photoion angular distributions, supporting their assignment to the same single-photon UV-induced photodissociation. Channel II exhibits a delayed appearance relative to Channel I, implying that, at earlier pump-probe delays where the iodine atom is close to the propyl fragment, CT is favored, but becomes improbable at longer pump-probe delays. This cessation of CT, heralding the formation of the low-momentum iodine ions of Channel II, was the primary focus of previous ultrafast CT studies [1], in which the direct signature of CT (Channel I) could not be resolved. As explored shortly, Channel I shares the dependence on ion charge state which has been viewed as characteristic of CT [1, 21].

The ability to observe Channel I in the current work is attributed to two factors. Firstly, the use of a weak-field UV pump pulse drives the excitation of a well-defined neutral dissociation. This is in stark contrast to initial experiments where strong-field pump pulses drove dissociative ionization, generating a large Coulomb explosion background [1, 18]. Secondly, by studying a larger molecule (C_3H_7I as opposed to CH_3I), there are more atoms to carry charge in XUV-only Coulomb explosions, reducing the one-color production of multiply charged I^{n+} ions [23, 35]. For example, a slight enhancement in the yield of high-KER I^{n+} ions shortly after time-zero was assigned to the presence of Channel I in a previous UV-XUV study on CH_3I (see Fig. 8 of Ref 23), but isolation (and thus further analysis) of the feature was not possible due to one-color background.

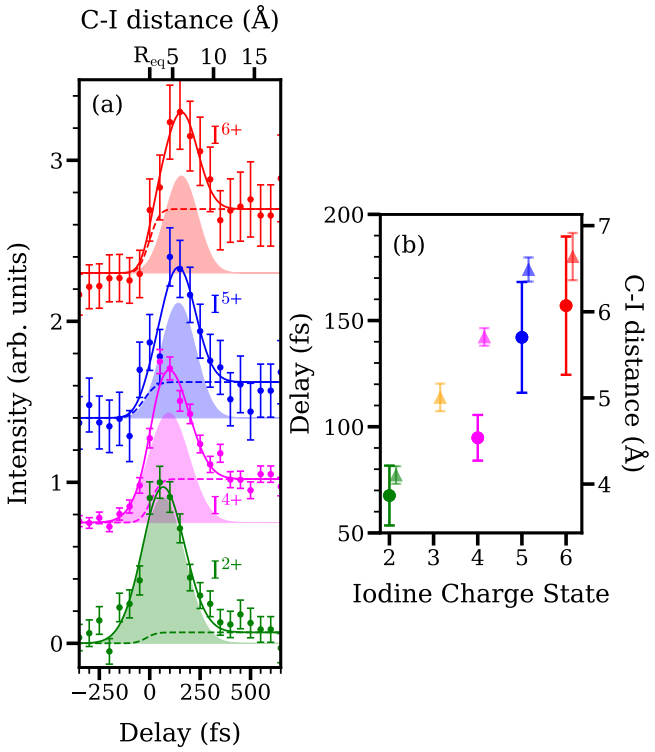

FIG. 2. (a) Integrated intensity of the background-subtracted delay-dependent I^{n+} ion momentum distributions for 120-300 a.u.(colored circles). For the I^{2+} ion, a narrower momentum range of 110 to 200 a.u. was used, to avoid overlap with probe-only signal. Intensities are normalized by their maximum value, and vertically offset. The total fit is plotted as a solid line. The two contributions to this fit, representing signal arising from Channels I and III are displayed as a shaded area and dashed line, respectively. (b) The centers of the Gaussian contributions (round marker) for each iodine charge state, with error bars corresponding to 1 standard deviation (1σ) of the fit parameter. The onsets of Channel II (triangular marker), determined by fitting solely to a normal cumulative distribution function, are shown for comparison.

Analyzing the Channel I signal in both the delay and momentum domains for each iodine charge state informs on how the time of XUV ionization affects the probability for CT, and the geometry at which the CT occurs. Figure 2(a) shows the delay-dependent intensities of high-momentum I^{n+} ions. These comprise a strong contribution from CT (Channel I), as well as a weaker contribution due to simultaneous photoionization at both I and C_3H_7 fragments by the XUV pulse (Channel III). The former process leads to an enhancement in the ∼0-300 fs range, whilst the latter is responsible for the increased signal which begins around time-zero and persists out to longer pump-probe delays.

If we assume a single value for the dissociation (i.e., C-I

bond extension) velocity following UV photoexcitation at time-zero, the delay axis can directly map to C-I bond length at the instant of inner-shell ionization [1]. This assumption of instantaneous acceleration introduces little error, owing to the very repulsive PESs involved in the photodissociation which cause rapid (∼few tens of fs) acceleration to the asymptotic dissociation velocity [26, 36]. Several interesting features can be observed in Fig. 2. Firstly, the CT peaks shortly after time-zero, at which point significant UV-induced bond extension has already occurred (cf. the ground state equilibrium bond length of ∼2.2 Å). Secondly, the peak in intensity of Channel I is narrow in time (200-300 fs FWHM), and shifts to longer pump-probe delays with increasing charge state n. To examine this trend further, we fit the traces in Fig. 2(a) to a two-component function: i) a Gaussian representing the transient enhancement due to Channel I and ii) a normal cumulative distribution function (CDF), representing the step-like enhancement due to Channel III.

Fig. 2(b) shows that the center of the Gaussian contribution shifts to longer pump-probe delay/C-I bond distances as iodine charge state increases. A corresponding shift in the onset of Channel II (triangular markers in Fig. 2(b) is also observed, in accord with previous studies [1, 21]. The temporal width of the Gaussian contribution at high ion momentum (i.e., the shaded contribution in Fig. 2(a)) is independent of charge state (within fitting error), indicating that within the constraints of the experimental time resolution (∼120 fs FWHM), the geometric 'window' (i.e. the range of C-I distances at the point of ionization) for CT is approximately equal for each I^{n+}, and it is this entire 'window' which shifts to more extended geometries as n increases.

The precise momentum of the I^{n+} fragments from Channel I encodes information about the molecular geometry at which electron transfer occurred. Under the assumptions of a classical Coulombic repulsion of two point charges between the I^{n+} ion and a singly-charged propyl cofragment, and a single dissociation velocity, an ion's momentum can be transformed directly to a separation between two repelling charges.

We note that such analysis neglects motion in dimensions other than the C-I coordinate and assumes that the Coulombic repulsion can be adequately described by considering two point charges, with the charge of the $C_3H_7^+$ species located on the central carbon atom. The assumption of purely Coulombic repulsion does not generally perform well at short internuclear distances, where the polycation PESs include contributions from valence bonding interactions [37–41]. However, as the CT and subsequent Coulomb explosion happens at extended geometries, the interactions can be well-approximated as those of point charges. Similarly, photoinduced vibrational motion in other coordinates (such as umbrella mode of the propyl radical [26]) is not expected to significantly alter the Coulomb repulsion at the level of sensitivity of the present experiment.

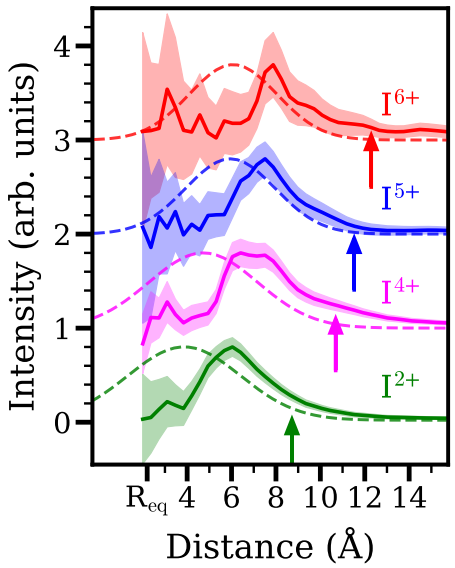

FIG. 3. Yield of Channel I as a function of charge separation as extracted from the I^{n+} ion momentum distributions. These distributions are vertically offset and each normalized by their maximum value. The shaded regions represent estimated 1σ error bars. The relevant critical distance predicted by the over-the-barrier model for the $I^{(n+1)+}$+C_3H_7 to I^{n+}+$C_3H_7^+$ CT process for each charge state n is indicated by a colored arrow. For comparison, the Gaussian distributions of C-I internuclear distances extracted from the delay-domain analysis shown in Fig. 2 are reproduced as dashed lines.

Figure 3 displays early-time (0-300 fs) ion momentum distributions, following transformation to a charge separation assuming Coulombic behavior. Contributions from Channel III have been subtracted, as described in Appendix H, leaving signal arising solely from Channel I. Here, comparison is drawn to the 'critical distance' predicted by the over-the-barrier model. This distance, at which the Coulombic barrier to electron transfer exceeds the valence electron binding energy and so CT is 'classically forbidden', increases with higher iodine charge state due to a deeper Coulombic well [1, 19, 20, 42] (as shown in Fig. 12 of Appendix E). This comparison highlights observed details of the CT behaviour which cannot be adequately described by this simple model. For instance, in many cases (particularly the higher charged iodine ions), CT has essentially halted before the predicted critical distance, and has a well-defined peak over a narrow region of charge separation, below which single CT is not observed.

Further comparison is drawn to the analysis in the pump-probe delay domain (the shaded contributions to the fits shown in Fig. 2(a), which are reproduced in Fig. 3 as dashed lines), which relates the intensity of Channel I to the C-I distance at the point of ionization (rather than at the point of CT). The momentum-domain analysis

yields much narrower distributions, as the geometric information is no longer restricted by the experimental time resolution. The direct comparison shows that, on average, the C-I bond is more extended at the point of CT than at the point of ionization. This observation, which was inaccessible by previous studies, implies that there may be a small time delay between ionization at the I atom and CT, during which the two fragments continue to recoil along the dissociation coordinate. These observations are consistent with CT being mediated by crossings between PESs which occur at specific geometries with more extended C-I bond distances, as discussed shortly.

Whilst the cessation of CT (i.e. onset of Channel II signal) has been probed by previous work involving time-resolved site-selective ionization [1], the present studies provide the first direct measurement of the entire window over which single CT occurs. The signature of CT is absent at the smallest pump-probe delays (smallest C-I bond extensions). This behavior can be interpreted in terms of differing stages in the transition from an intact molecule to isolated photofragments following UV excitation. At sufficiently large C-I bond extension, charge is localized at the isolated iodine atom following ionization. When the C-I bond distance is close to its neutral ground state equilibrium value, XUV ionization again proceeds from the I 4d orbital, but the AM relaxation is molecular in nature, and leads to Coulomb explosion behavior similar to that of the unpumped molecule, in which multiple carbon- and/or hydrogen-containing ionic fragments are produced [35]. Between these two regimes ionization and AM decay is localized at the iodine atom, but the distance from the iodine to the recoiling neutral propyl fragment is small enough that single electron transfer from the propyl is possible. At the shortest pump-probe delays, we appreciate that multiple CTs could conceivably also play a role and persist out to longer pump-probe delays for higher iodine charge states, though the present experiments do not show any clear signatures of such processes. The persistence of multiple CT out to longer pump-probe delay/internuclear distance for higher iodine charge state may explain the observed charge-state-dependent shift in the onset of single CT. In future studies, the incorporation of coincidence or covariance [35] ion detection would be valuable, to distinguish I^{n+} ions formed in the same process as singly charged propyl ions (or their daughter fragments) from those formed with smaller fragment ions that derive from the decay of propyl polycations (the signature of multiple electron transfers).

CT cross-sections, particularly at low collision energies, are dominated by non-adiabatic effects at the crossings of PESs [19, 43]. Many such surface-crossings can contribute to a given CT process, populating a series of electronically excited (Rydberg) states in the polycation accepting the transferred electron (as discussed in more detail in Appendix J). Future work may be able to 'map out' these regions of non-adiabaticity through complementary delay-dependent measurements on the electronic state of the product I^{n+} ions. Identification of specific electronic pathways through which CTs operate might be achieved through measuring fluorescence spectra of the I^{n+} ions, as reported extensively for collision-induced CT [44–48]. A number of methods exist for predicting the n and l propensities for Rydberg states formed in charge-exchange collisions [20, 44]. In a photodissociating system, however, the motions of the participating systems are much more constrained; the two moities travel away from one another, initially from a very small separation and with a well-defined relative orientation. Such simplicity is in marked contrast to the colliding systems, where the partners first approach from long distance, with a range of impact parameters, and reach some minimum distance of approach before travelling apart again. It is this difference in motions, and the ability for dissociation to be induced at a specific delay before site-selective ionization which could enable new regimes of CT physics to be accessed in these emerging ultrafast pump-probe measurements.

In conclusion, we present an experimental study of CT processes initiated by site-selective inner-shell ionization during a neutral photodissociation. A clear signature of the Coulombically repelling fragments formed by CT between the selectively ionized iodine atom and the recoiling alkyl radical is identified. This CT occurs over a small window of C-I separations which is significantly extended from the equilibrium geometry and shifts to greater internuclear distances for higher I^{n+} charge states. This geometric window corresponds to intermediate behavior in the electronic relaxation dynamics following I 4d ionization between the limits of an isolated iodine atom (at large C-I distance) and that of a bound molecule (at the equilibrium C-I distance), at which point interfragment electron transfer can occur. The propensity for CT to occur over a narrow region of C-I internuclear separation can be understood in terms of couplings between PESs at these specific geometries which mediate CT. We see compelling evidence that, if multiple ionization occurs in the dissociating system at shorter internuclear distances, CT may be delayed until these regions of strong coupling are reached. Future experiments in which photoions and AM electrons are recorded simultaneously and analyzed in coincidence or covariance [36, 49] would be of particular interest to study transient electronic structure changes, as too would the detection of fluorescence produced by radiative relaxation of the electronically excited I^{n+} species produced [44–48].

ACKNOWLEDGMENTS

The experiment was performed at SACLA with the approval of JASRI and the program review committee

(proposal No. 2021A8038 Forbes). We thank the technical and scientific staff of SACLA for their hospitality and support before and during the beamtime. R.F. and F.A. gratefully acknowledge support from the Linac Coherent Light Source, SLAC National Accelerator Laboratory, which is supported by the US Department of Energy, Office of Science, Office of Basic Energy Sciences, under contract no. DE-AC02-76SF00515. D.R. and A.R. were supported by contract no. DE-FG02-86ER13491 from the same funding agency. J.W.L.L. acknowledges financial support via the Helmholtz-ERC Recognition Award (ERC-RA-0043) of the Helmholtz Association (HGF). B.D.W. thanks the CLF and the University of Southampton for a studentship. R.S.M. thanks the EPSRC for financial support (EP/R010609/1). J.M., M.Bro., D.M., D.H., P.A.R., C.V. and A.J.O.E. gratefully acknowledge the support of EPSRC Programme grant EP/V026690/1. M.Bu. and T.W. are also grateful to EPSRC for support from EP/S028617/1. T.W. is additionally thankful to EPSRC for studentship funding and Jesus College, Oxford for a partial fee scholarship. P.H.B., A.J.H. and M.Bri. were supported by the National Science Foundation. J.N. acknowledges Academy of Finland funding via project 331234. Y.K. acknowledges support by JSPS KAKENHI Grant No. 20K14427.

Appendix A: Experimental Details

The experiment was performed at the XUV beamline (BL1) of the SACLA free-electron laser [25]. FEL pulses at a photon energy of 95 eV (13.1 nm wavelength) were generated at 60 Hz, with estimated duration of ∼30 fs [51]. The XUV pulses were attenuated with a 650 nm thick Zr filter, prior to focusing to a spot size of $\sim 10\mu$m ($1/e^2$) at the interaction point in the spectrometer. The shot-to-shot FEL pulse energies were measured upstream of the experiment using a gas intensity monitor [52], with a mean value of ∼30 μJ [25]. Accounting for expected transmission of the beamline (∼90%) and the solid filter (∼11%), we estimate an on-target pulse energy of 3 μJ and a peak intensity of $\sim 2.5\times10^{14}$ W/cm^2.

The UV pump pulses were generated by frequency tripling the output of the BL1 optical laser system, which comprised a Ti:sapphire oscillator (Vitara, Coherent Inc.), a chirped-pulse regenerative amplification system (Legend Elite, Coherent Inc) and a home-built multipass amplifier [25]. This system is capable of producing ∼10 mJ 800 nm pulses, but in the current experiment far lower pulse energies were employed. Prior to frequency tripling, the fundamental was attenuated by a computer-controlled variable neutral density filter to give UV pulses of a suitable energy, which was 5 μJ in the current experiments. The UV pulses were focused into the interaction region with a 2 m focal length lens. The incoming UV laser beam was overlapped with the FEL in a nearly collinear geometry using a right angle prism mirror. The delay between the optical laser and FEL was scanned using a computer-controlled motorized delay stage. On a single shot basis, the jitter between the two pulses was measured using an arrival time monitor [32], and ultimately the data was rebinned following correction of this jitter.

The velocity-map imaging spectrometer used in the experiment has been described in detail previously [31], and has been employed in several experiments at the SACLA facility [18, 35]. Room temperature 2-iodopropane vapor was expanded as a neat supersonic molecular beam through a pulsed General Valve. The beam was passed through a skimmer into the interaction chamber, where it was intersected by the laser and FEL beams at a crossing angle of approximately 45 degrees. Generated ions were accelerated by a series of electrodes under velocity-mapping conditions [30] to a time- and position- sensitive detector consisting of dual MicroChannel Plate MCP and a hexanode delay-line. From the measured arrival time and hit positions, the 3D momentum information of each detected ion event could be determined.

Appendix B: Time-resolved ion momentum distributions

Figures 4 and 5 display the time-resolved momentum distributions for the I^{2+} to I^{6+} ions. Figure 4 presents the 'raw data', whilst in Fig. 5 a background subtraction has been performed to further isolate the pump-probe features of interest. For this purpose, the momentum distribution for data between -1000 and -200 fs (i.e. UV late) was averaged, scaled by 90% (to account for an estimated fraction of 10% molecules being pumped by the UV laser) and subtracted from the momentum distribution at each pump-probe delay. This background subtraction is only of significance for the I^{2+} ion, where there is a considerable background from XUV only ionization of unexcited molecules in the 200 to 300 a.u. region. In order to effectively isolate the pump-probe signals of interest, the background-subtracted data are used throughout the main manuscript.

The higher momentum region of the I^{3+} ion is contaminated slightly by contributions from the $C_3H_6^+$ and $C_3H_7^+$ ions, due to their very similar mass-to-charge ratios (42.3 for I^{3+}, 42 and 43 for $C_3H_6^+$ and $C_3H_7^+$ respectively). For this reason, the I^{3+} ion was excluded from much of the main analysis. The exception to this is the analysis of the low momentum feature (Channel II), which is spread over a narrow distribution of detector arrival times and positions, and thus is not contaminated by these overlapping contributions.

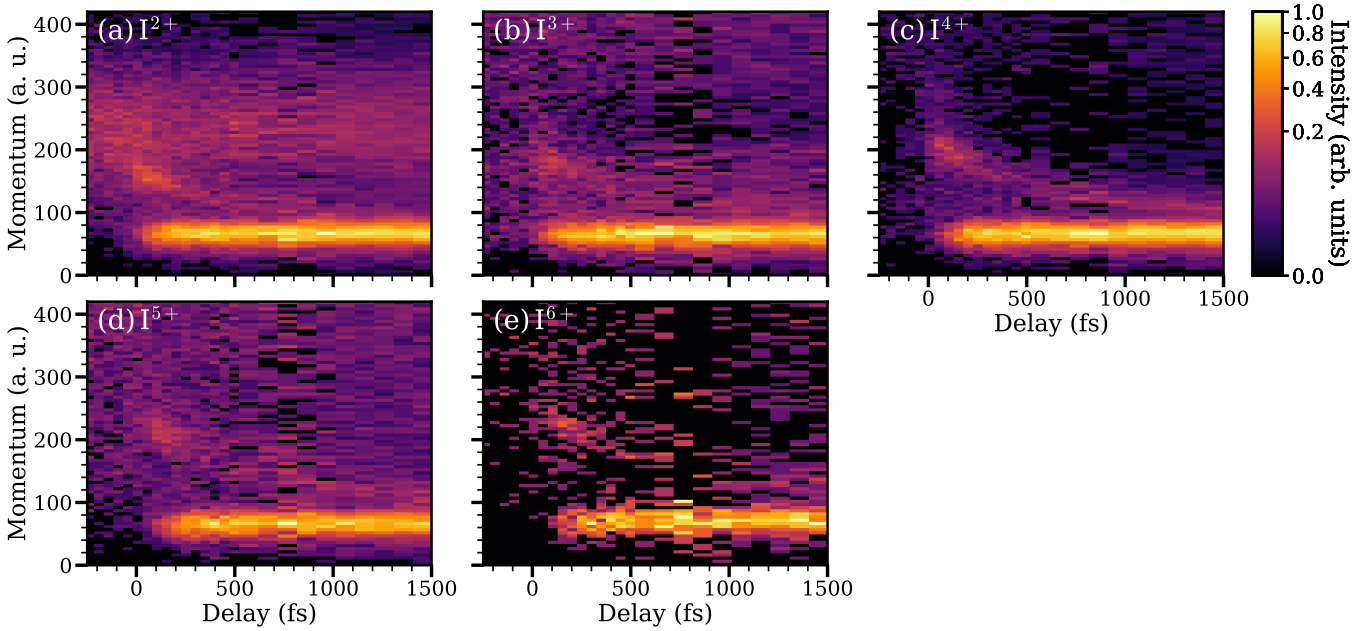

FIG. 4. Delay-dependent ion momentum distributions for I^{2+} to I^{6+}. No background subtraction has been performed on these data.

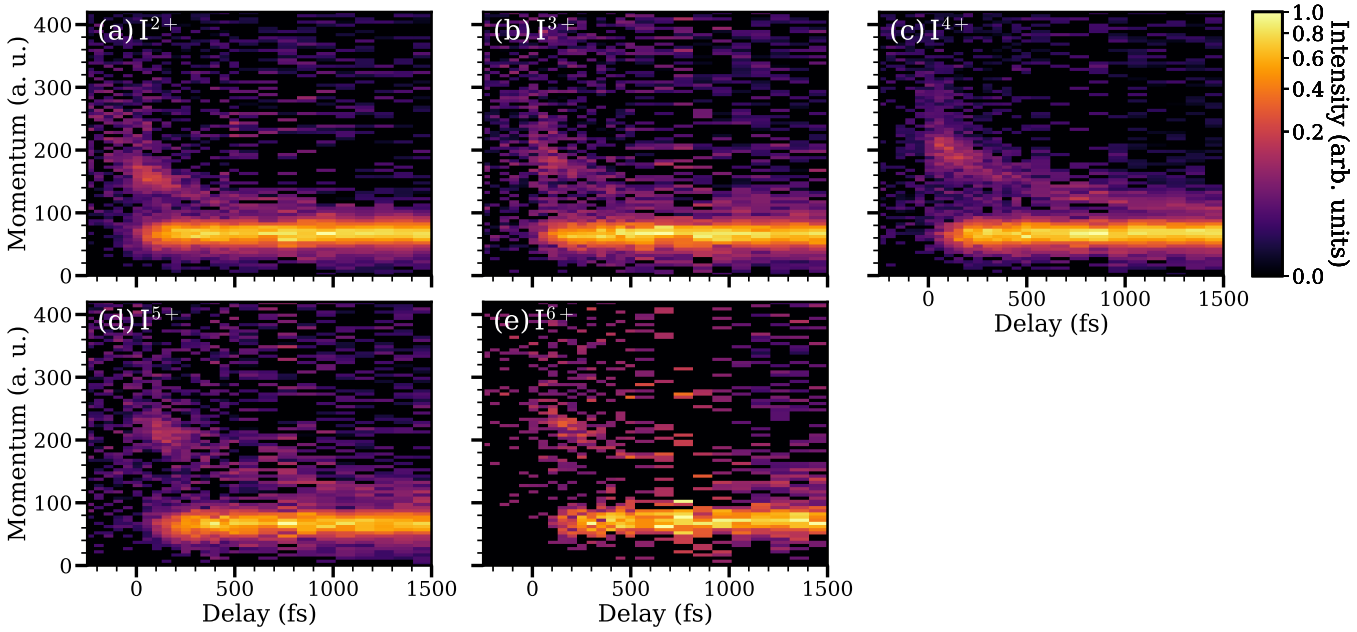

FIG. 5. Delay-dependent ion momentum distributions for I^{2+} to I^{6+}. A subtraction of the UV-late background has been performed, as discussed in the text.

Appendix C: Channel Assignment

In order to make and confirm the assignments of the different pump-probe channels observed in the experiment, a series of further analyses were performed. Firstly, to confirm the assignment of Channel II to neutral UV-induced dissociation prior to localized ionization at the iodine site, we compare the measured iodine KER distributions to those reported in the literature [26]. An example of this analysis is shown for the I^{4+} ion in Fig. 6(b). The KER distribution extracted from the current experiment for pump-probe delays between 100 and 500 fs is plotted in red. The KER distribution obtained at late pump-probe delays agrees well with the femtosecond (i.e. non I/I* state selective) Resonance-Enhanced Multiphoton Ionization

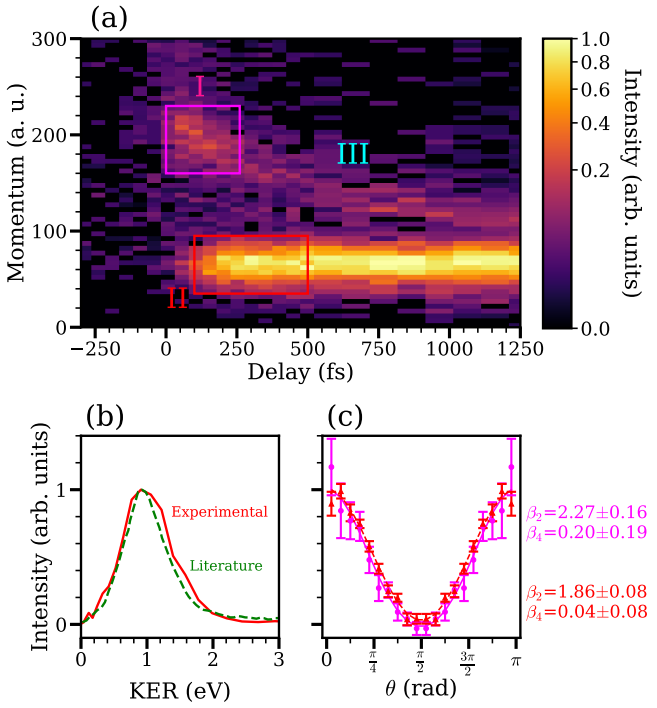

FIG. 6. Additional analysis supporting the present channel assignments, shown for the I^{4+} ion as an example. (a) Delay-dependent I^{4+} ion momentum distribution. (b) Comparison between the kinetic energy release (KER) distributions extracted from the present data in the long delay limit (blue solid) compared to literature measurements (green gashed) [26]. (c) Comparison of the laboratory-frame angular distributions associated with (and color coded to match) the regions-of-interest marked in panel (a). For the high- and low-momentum regions-of-interested, experimental data is plotted as circular and triangular markers, respectively. Fits to these distributions are shown as solid and dashed lines, respectively, as are the β parameters extracted from these fits.

(REMPI) results from Bañares and coworkers [26] and with that reported for the (dominant) I fragments measured by nanosecond REMPI following excitation of 2-iodopropane at the same wavelength [53]. A slightly broader KER distribution is seen in the present experiment, which is believed to be due to poorer velocity resolution compared to the literature work.

To confirm the assignment of Channel I to single-photon UV photodissociation, but following XUV-induced charge transfer, the laboratory-frame angular distributions (i.e. ion signal as a function of angle with respect to the polarization axis of the UV laser) for Channels I and II are compared. This is done by isolating signal associated with the regions of interest in time and momentum as indicated in Fig. 6(a). These two angular distributions are compared in Fig. 6(c). As expected, the two angular distributions are similar, indicative of them sharing a common origin. Also shown in Fig. 6(c) is the result of fitting the photoion angular distribution, $I(\theta)$ to:

$$I(\theta) = (\sigma/4\pi)[1 + \beta_2 P_2(\cos\theta) + \beta_4 P_4(\cos\theta)] \qquad \text{(C1)}$$

where $P_n(\cos\theta)$ is the nth Legendre polynomial in $(\cos\theta)$. A β_2 value of close to 2 is observed, as expected given in the parallel nature of the UV transition, and as has been measured previously [27]. The observation of a value close to zero for β_4 confirms that both these channels are dominated by absorption of a single UV photon, as expected.

Figure 7 shows four-fold symmetrized images of the I^{4+} ion in the detector plane at a series of pump-probe delays. Here, the significantly greater momentum associated with Channel I is clearly visible in panel (b), as is the qualitative similarity in angular distribution to Channel II, which has a significantly lower radius and persists out to long pump-probe delays.

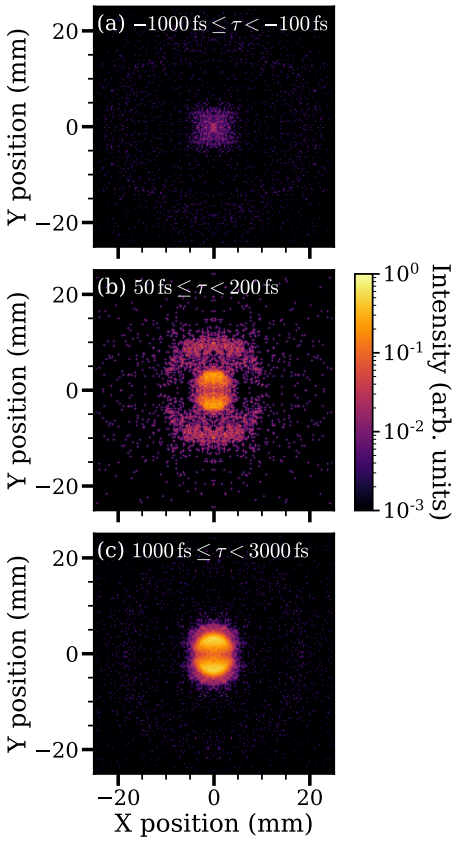

FIG. 7. Detector plane symmetrized velocity-map images for the I^{4+} ion, integrated over its entire time-of-arrival spread, plotted on a logarithmic color scale as indicated. (a) UV late (-1000 fs to -100 fs), (b) UV just early (+50 fs to +200 fs), (c) UV very early (+1000 fs to +3000 fs).

Appendix D: Fitting of Time-resolved Ion Yields

Figure 8 panels (a) through (d) show the results of the fits to the delay-dependent intensity of ions produced in the high momentum region for the I^{2+} to I^{6+} (excluding I^{3+}) ions. For I^{4+} to I^{6+}, a range of 120 a.u. to 300 a.u. was used to define this high momentum region. For the I^{2+} ion, a narrower and lower range of 110 a.u. to 200 a.u., to avoid significant overlap with the probe-only signal. These definitions are used throughout the analysis shown in the main Manuscript and Appendices.

In these plots, the solid black line is a Gaussian representing the contribution of Channel I, whilst an additional normal cumulative distribution function (CDF), plotted as a dashed black line, represents signal arising from Channel III. The solid colored line is the sum of these two contributions, which in all cases matches well with the experimental data (colored points). In addition to the general trend that the Gaussian peaks at longer delays for higher charge states, as discussed previously, an additional general trend is seen, namely the increasing weight of the cumulative distribution function for higher charge states. This can be seen in Fig. 9, which shows various fit parameters as a function of iodine charge state. The increasing contribution from the cumulative distribution function is because Channel III, which involves XUV ionization at both the iodine and propyl sites becomes increasingly likely for the highest XUV intensities sampled in the experiment. As producing higher iodine charge states involves absorption of multiple XUV photons, data for higher charge states is dominated by contributions from the highest XUV intensities sampled in the experiment (i.e., closer to the peak of the XUV focus). Similar behavior, in which ionization at an isolated hydrocarbon fragment was more probable in coincidence with higher iodine charge states, was observed in a previous pump-probe study on CH_3I employing ionization by intense XUV pulses [18].

Figure 10 displays the integrated intensity of low momentum (40 a.u. to 80 a.u.) I^{2+} to I^{6+} ion signals as a function of pump-probe delay. These data are fit to a single normal CDF, as has been performed in the literature [1, 18, 22]. This CDF function used in the fitting, as a function of pump-probe delay t, takes the form:

$$C(t) = \frac{A}{2}\left(1 + \mathrm{erf}\left(\frac{t - t_{\mathrm{CDF}}}{\sqrt{2}\sigma_{\mathrm{CDF}}}\right)\right) + B \qquad \text{(D1)}$$

where t_{CDF} and σ_{CDF} are the center and width of the distribution, respectively. A represents the asymptotic upper limit of the function, while B is the asymptotic lower limit. The error function, erf is defined as:

$$\mathrm{erf}(z) = \frac{2}{\sqrt{\pi}}\int_0^z e^{-w^2} dw \qquad \text{(D2)}$$

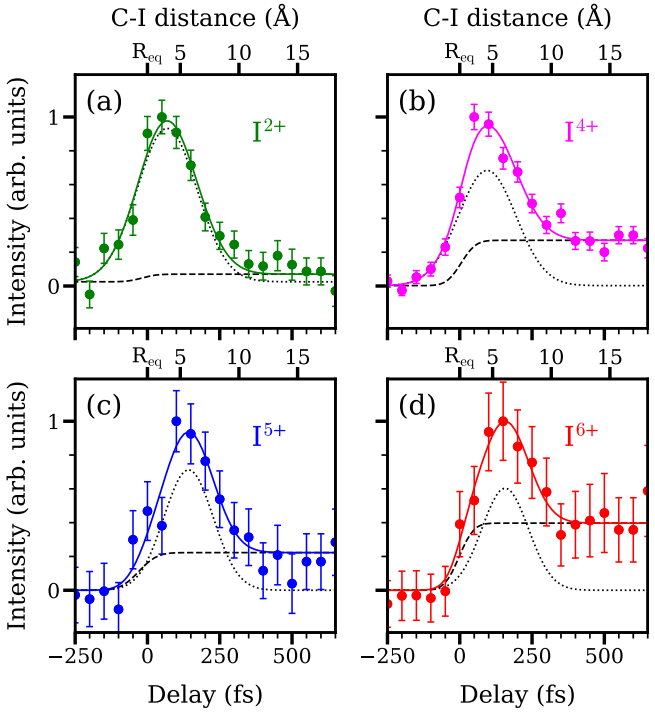

FIG. 8. Fitting of the delay-dependent intensity of higher momentum I^{n+} ions. Experimental data are shown as colored circle markers. The total output of the fit is represented by the solid colored lines, while the Gaussian and CDF contributions are plotted as dotted and dashed black lines, respectively.

The resulting fit parameters, namely the center and width of the CDF are plotted in Fig. 11 panels (a) and (b) respectively. As observed previously [1, 18, 22] the center of the CDF shifts to later delays as iodine charge state increases, consistent with charge transfer occurring out to longer delays and greater internuclear separations.

Appendix E: Classical Over-the-barrier Model

As discussed in the main manuscript, charge transfer involving highly charged species is often discussed in relation to a 'critical distance' predicted by a classical over-the-barrier model of the charge transfer process [1, 19, 20]. Within this model, charge transfer is assumed to be 'allowed' if the potential barrier separating the two charge sites does not exceed the binding energy of the electron to be transferred (in the case considered in the present work, this comes from the neutral propyl radical). The Coulombic potential, $V(r)$, for electron transfer from a site A to a site B, with charges P and Q respectively, separated by an internuclear distance r_{AB} is given by:

$$V(r) = -\frac{(P+1)}{(r - r_{\mathrm{AB}})} - \frac{Q}{r_{\mathrm{AB}}}\,. \qquad \text{(E1)}$$

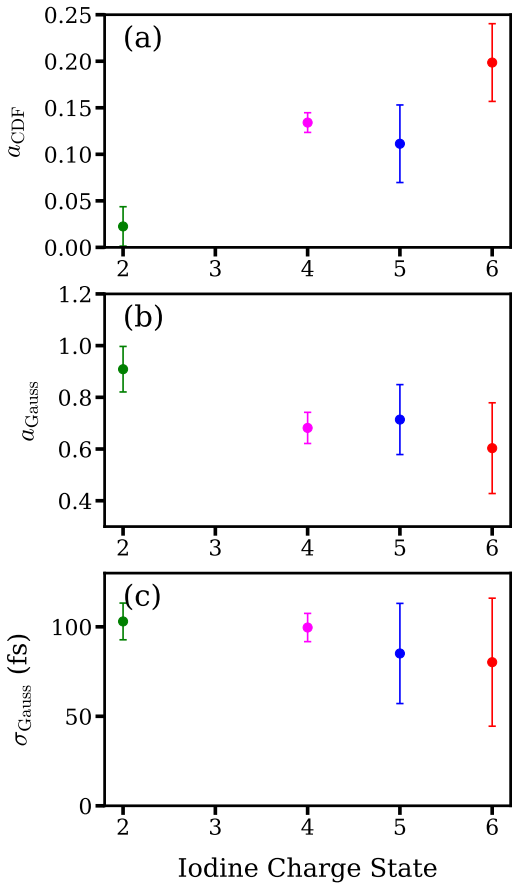

FIG. 9. Comparison of parameters from the fitting of the delay-dependent high momentum ion yields. Panels (a) and (b) show the amplitudes of the cumulative distribution function (a_{CDF}) and Gaussian function contributions (a_{Gauss}), respectively, whilst panel (c) shows the width (standard deviation) of the Gaussian contribution (σ_{Gauss}).

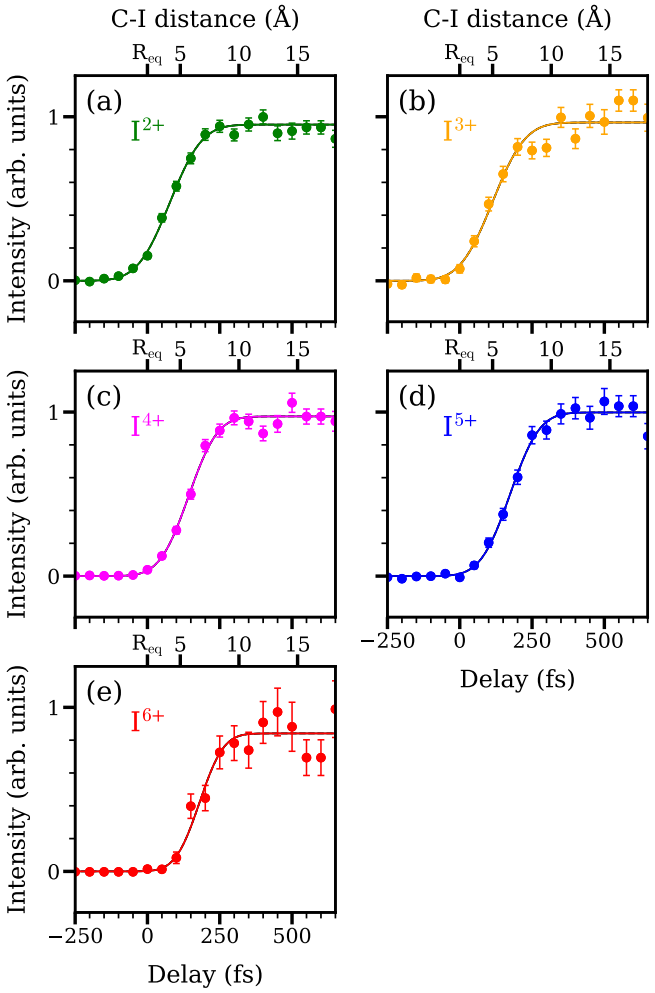

FIG. 10. Fitting of the delay-dependent intensity of low momentum (i.e. Channel II) I^{n+} ions. Experimental data are shown as colored circle markers. Output of the fits are shown as colored solid lines.

Figure 12 shows this potential for the case of a charge transfer between I^{4+} and neutral C_3H_7 for a series of internuclear distances. At the 'critical' internuclear distance (Fig. 12 (b)), the barrier between to electron transfer is equal to the binding energy of the C_3H_7 radical's valence electron, and so beyond this (Fig. 12 (c)), charge transfer can be thought to be forbidden. It can be shown that the critical distance, r_{crit} for a specific charge transfer process is given by:

$$r_{\mathrm{crit}} = \frac{(P+1) + 2\sqrt{(P+1)Q}}{\mathrm{IE_A}}, \qquad \text{(E2)}$$

where $\mathrm{IE_A}$ is the ionization energy of A.

Table I lists these critical distances for different charge transfer processes of relevance to the current work, calculated using Equation E2, assuming A=i-C_3H_7 radical with an IE of of 7.37 eV [54, 55].

Charge Transfer Pathway	r_{crit} / Å
$I^{2+}+C_3H_7 \rightarrow I^{+}+ C_3H_7^{+}$	7.48
$I^{3+}+C_3H_7 \rightarrow I^{2+}+ C_3H_7^{+}$	8.72
$I^{4+}+C_3H_7 \rightarrow I^{3+}+ C_3H_7^{+}$	9.77
$I^{5+}+C_3H_7 \rightarrow I^{4+}+ C_3H_7^{+}$	10.69
$I^{6+}+C_3H_7 \rightarrow I^{5+}+ C_3H_7^{+}$	11.52
$I^{7+}+C_3H_7 \rightarrow I^{6+}+ C_3H_7^{+}$	12.29

TABLE I. Critical distances for different charge transfer processes, as predicted by the classical over-the-barrier model.

Appendix F: Delay-Dependent Yields of High and Low Momentum Ions

Figure 13 compares the delay-dependent ion yields of low and high momentum ions for each iodine charge state. It can be seen that, as mentioned in the main manuscript,

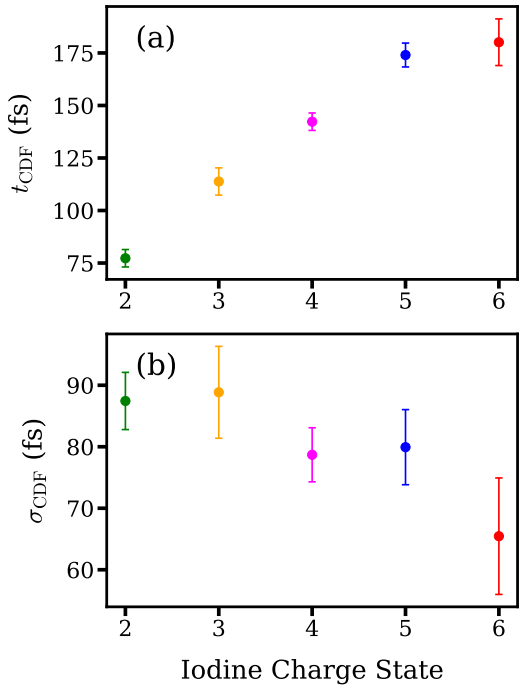

FIG. 11. Comparison of parameters from the fitting of the delay-dependent low momentum ion yields. Panels (a) and (b) show the center (t_{CDF}) and width (σ_{CDF}) of the cumulative distribution function.

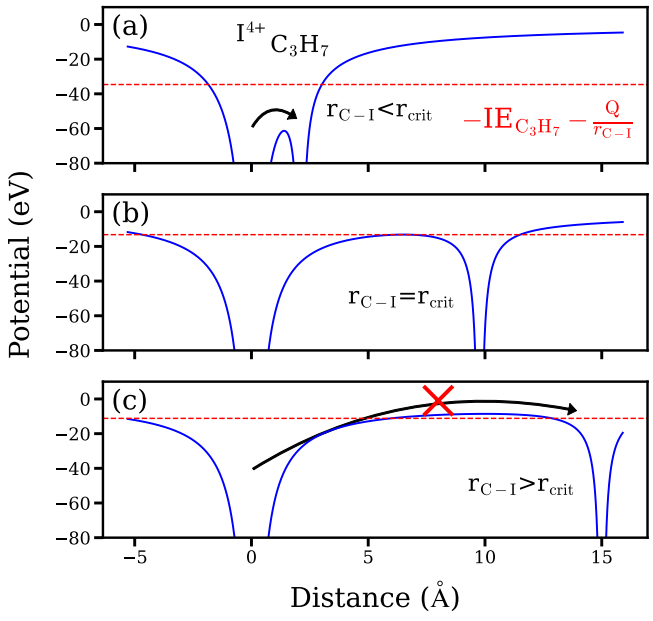

FIG. 12. Example Coulombic potentials formed for a I^{4+} ion and neutral C_3H_7 fragment at a range of internuclear distances, r_{AB} relative to the critical distance r_{crit}: a) $r_{C-I} < r_{crit}$, b) $r_{C-I} = r_{crit}$, c) $r_{C-I} > r_{crit}$. The red dashed line represents the valence electron binding energy of the C_3H_7 radical. At internuclear distances beyond the critical distance, the barrier to electron transfer exceeds the valence binding energy and electron transfer is classically forbidden.

the signal at lower momentum rises at longer delays than the higher momentum signal. This is expected, as the low momentum signal (Channel II) only dominates once the charge transfer probability declines (i.e. at greater interfragment separations). We note here, that there appears to be a 'shoulder' in the rise of intensity of the high momentum ions in some ions at short times, particularly in I^{5+} and I^{6+}. This is due to the increased prominence of Channel III in these ions, which rises in intensity at approximately time-zero.

Another potentially insightful comparison is to compare the timescale of Channel I for a given I^{n+} ion to that of Channel II for $I^{(n+1)+}$. This is because high energy I^{n+} ions are attributed to a charge transfer, originating from $I^{(n+1)}$. As such, one would expect that the intensity of Channel II in $I^{(n+1)}$ would rise at the same pump-probe delays as the intensity of Channel I in I^{n+} declines. Figure 14 shows this comparison, which is consistent with our interpretation of these delay-dependent signals.

Appendix G: Classical Time-resolved Coulomb Explosion Modelling

To aid analysis and interpretation of the data, simple classical simulations of observed time-resolved Coulomb explosion signals were performed. In particular, these simulations were used to analyse the weak signal coming from ionization at both the I and C_3H_7 fragments formed by UV dissociation (Channel III). For the simulations, a number of trajectories were simulated, assuming constant (asymptoptic) UV-induced dissociation velocities between recoiling fragments, as sampled from the measured velocity distribution of I^{2+} ions at long pump-probe delays (i.e., Channel II). For each trajectory, a Coulombic contribution to the I^{n+} KE was added at each of a set of pump-probe delays, assuming classical Coulombic repulsion between two point charges, with a charge of $(n+)$ located at the iodine atom, and a single charge located at the central carbon of the C_3H_7 moiety. Finally, the data were convoluted in momentum and pump-probe delay by the estimated experimental momentum and time resolutions, respectively, to yield delay-dependent momentum distributions which could be compared directly to experiment.

In the experimental data, there is no clear transient signal which arises when the UV and XUV pulses are overlapped in time, as has been observed in previous experiments of this type [22, 23]. In order to establish the time at which the two pulses are overlapped ('time-zero'), without making any assumptions about the charge transfer processes occurring close to time-zero, the signal associated with Channel III at longer pump-probe delays was examined. As at longer pump-probe delays, the KE of this channel can be well reproduced by the previously described classical model (as has been observed in other

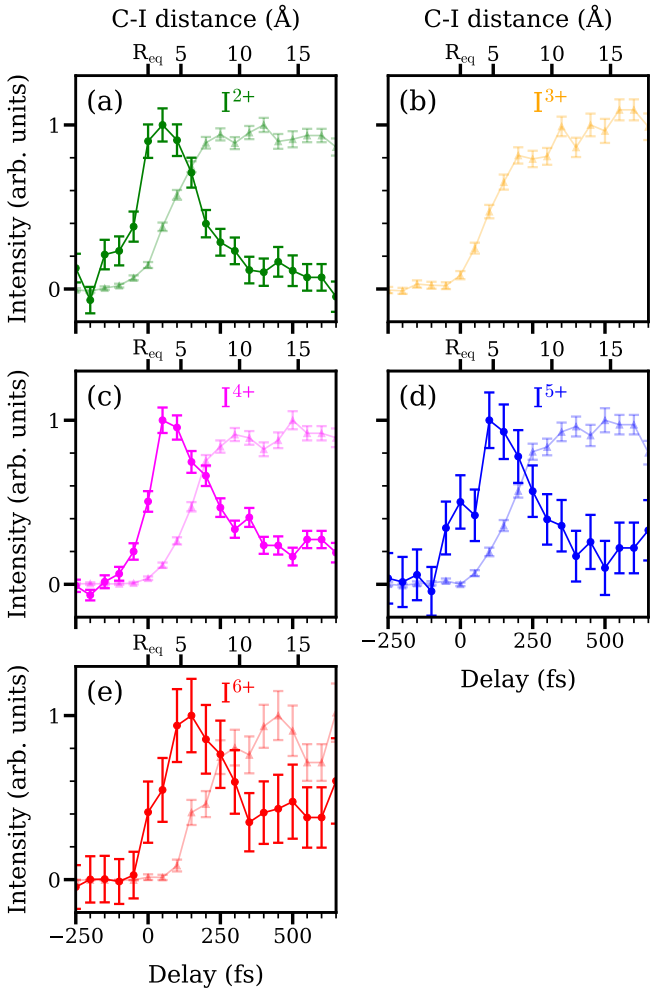

FIG. 13. Comparison of the timescales of formation of low- and high- momentum ions of the same charge state. For each iodine charge state, the yields of high momentum ions are plotted as solid circles, while low momentum ions are plotted as partially transparent triangles.

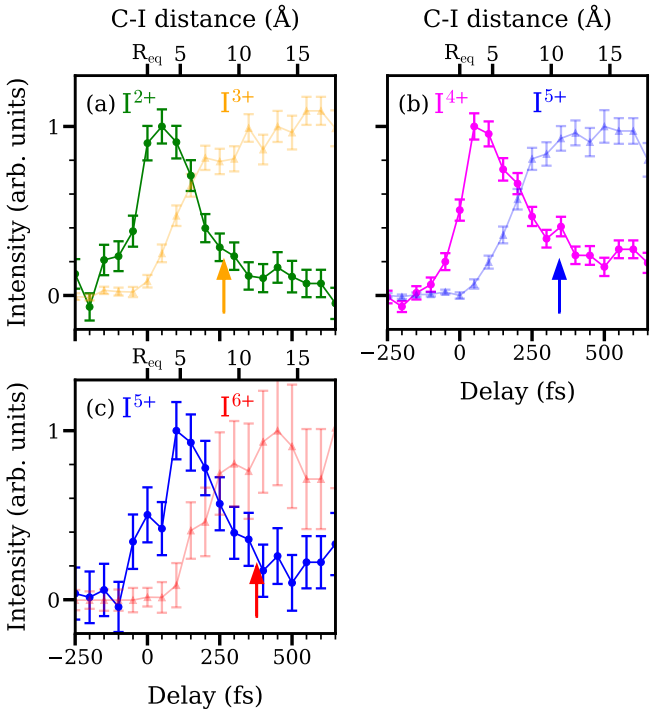

FIG. 14. Comparison of the timescales of formation of low- and high- momentum ions. Here, comparison is drawn between the high momentum I^{n+} and low momentum $I^{(n+1)}$ ions, due to their shared origin. For each iodine charge state, the yields of high momentum ions are plotted as solid circles, while low momentum ions are plotted as partially transparent triangles. The over-the-barrier model critical distance for the C_3H_7+$I^{(n+1)+}$ → $C_3H_7^+$+I^{n+} CT is shown as a colored arrow.

similar time-resolved Coulomb explosion experiments [18, 34]),the optimal time-zero was found that gave the best agreement between the simulated data and the signal associated with Channel III at these longer pump-probe delays. Figure 15 summarizes this procedure for the I^{4+} ion as an example, where the optimum agreement between the simulation and the observed signal in the range 100-200 a.u. and 300-1000 fs was found, and used as the time-zero in the experiment. Similar analysis for the I^{2+} ion yields the same value of time-zero.

Appendix H: Kinetic Energy Analysis of Charge Transfer

As discussed previously, the kinetic energies of ions produced following charge transfer encode information about the geometry of the system at the point of charge transfer. Figure 16 shows the steps in this data analysis procedure for the example of the I^{4+} ion, which are described in detail below.

Firstly, the experimental momentum distributions in the pump-probe delay region of interest (0-300 fs) were converted to a kinetic energy distribution, shown in Fig. 16 (a). Intensity for momenta below 100 a.u. was set to zero to remove contributions from Channel II. From these distributions, the mean kinetic energy of the UV photodissociation was subtracted, to leave solely Coulombic contributions to the kinetic energy, shown in Fig. 16 (b). A total KER of 0.95 eV was used for this analysis. The same dissociation KER, which corresponds to a relative recoil velocity of ∼2400 ms^{-1}, or fragment momentum of ∼64 a.u. was also used for the conversion from pump-probe delay to internuclear separation, as employed in Fig. 2 of the main manuscript.

Using Coulomb's law, these kinetic energies could then be transformed to a charge separation distance, assuming a singly charged propyl cofragment against which the I^{n+} repels, shown in Fig. 16 (c). Importantly, however, there are significant contributions from Channel III in these data, particularly in the higher charge states and

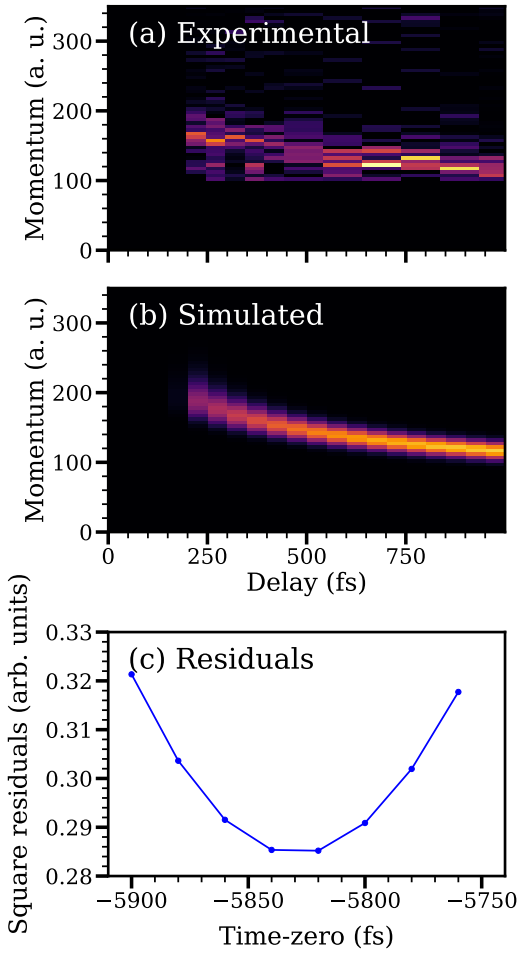

FIG. 15. Assignment of time-zero by comparison between simulated and experimental signals for the time-resolved Coulomb explosion imaging signal. (a) An example comparison between the experimental and simulated signal in the region of interest. (b) The summed square residuals between the experiment and the fit at a series of assumed experimental time-zero values. Note that these values are derived from the position of the motorized delay stage in the laser path, and exhibit some offset from the temporal overlap of the pump and probe pulses. Time-zero was assigned as the delay which gave the smallest squared residual.

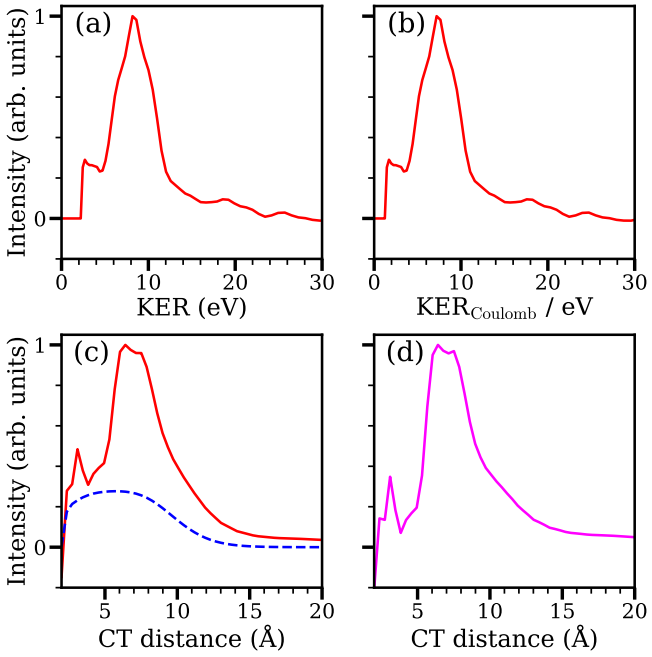

FIG. 16. Analysis of the short delay, higher momentum ion signals in charge separation space, shown for the I^{4+} ion as an example. (a) The KER distribution integrated over 0-300 fs. (b) The KER distribution after subtraction of the contribution from the UV-induced photodissociation. (c) Following conversion to a Coulombic charge separation. The simulated contribution from Channel III is shown as the blue dashed line. (d) Following subtraction of the simulated Channel III contribution from the experimental data.

especially at shorter charge separations. To isolate contributions from Channel I, the same analysis on the classical simulations of Channel III was performed (e.g., as already shown in Fig. 15), which give the distributions shown as dotted lines in Fig. 17. For the data presented in Fig. 3, these contributions were subtracted. The weighting used for this subtraction, relative to the main Channel I contribution, was taken from the previously described fits of the experimental high ion momentum data (i.e., using the amplitude of the CDF contribution shown in Fig. 9 for each ion).

In the above analysis, it is assumed that there is only a single KE due to the neutral photodissociation. In reality, the neutral photodissociation results in a distribution of kinetic energies, as shown in Fig. 6. In order to assess the impact on the above analysis, we turn once more to simple simulations of the experimental data, where a given charge-transfer distribution can be input into the simulation, and compared to that extracted by the above analysis procedure.

Expected signals for Channel I and II as a function of pump-probe delay were simulated under the assumptions of instantaneous acceleration to a constant dissociation velocity. This assumption broadly holds given the steeply repulsive potentials involved in the UV-induced photodissocaition. As shown previously through simulations on the related molecule 1-iodo-2-methylbutane, photodissociation velocities are expected to approach their asymptotic values in less than ∼30 fs (Fig. 10 in Ref. 36). Given our experimental resolution, we do not expect to be sensitive to deviations from this approximation of instantaneous acceleration. For each simulated trajectory, the final dissociation velocity was sampled from a Gaussian distribution, very similar to that observed experimentally. Additionally, a Gaussian distribution of charge-transfer probability was observed in interfragment separation. For a given charge state $I^{(n+1)+}$, if charge transfer occurs for a simulated trajectory, then an additional classical

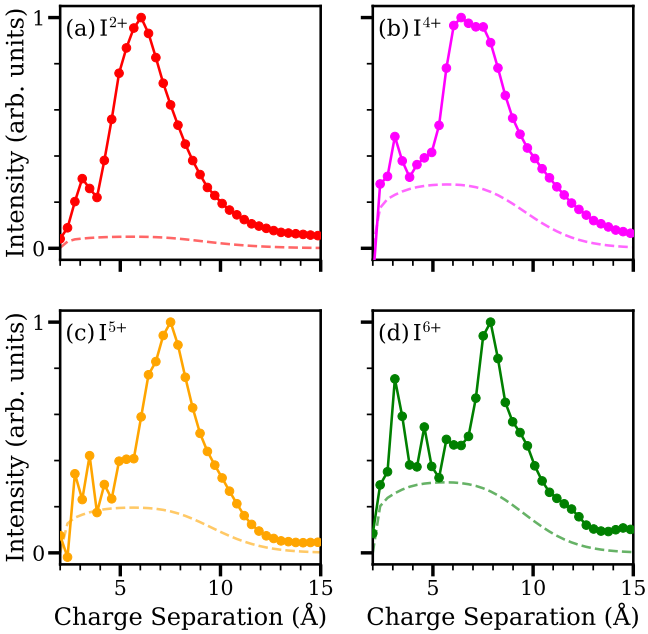

FIG. 17. Analysis of the short delay, higher momentum ion signals in charge separation space. For each ion, the experimental signal is shown as a solid, colored line, whilst the simulated background arising from Channel III is shown as a dashed line. In Fig. 3 of the main manuscript, this simulated background contribution has been subtracted

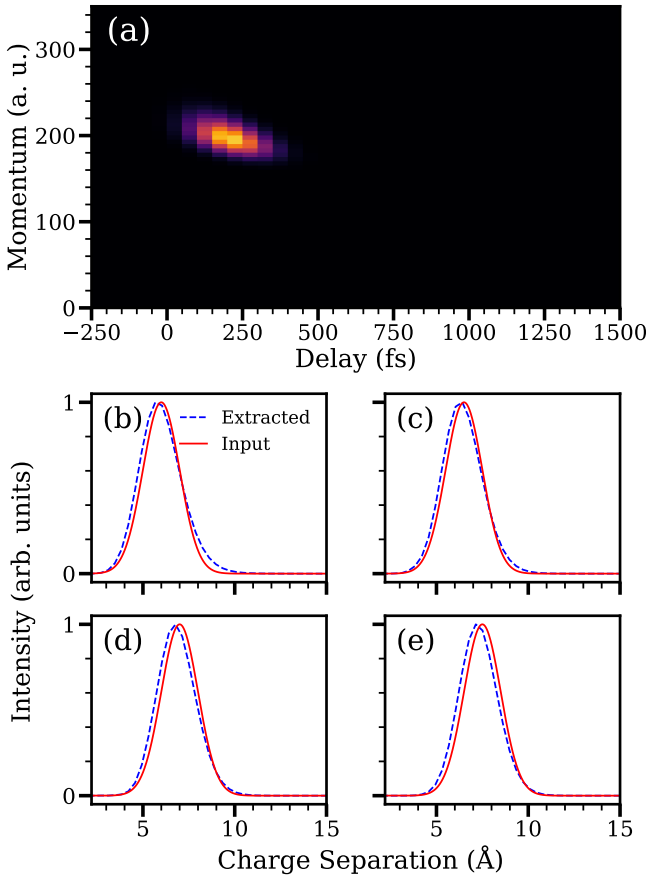

FIG. 18. Example demonstration of the extraction of charge separation information on simulated data. (a) Simulated signal for Channel I of the I^{4+} ion, for a given assumed charge separation distribution. (b) to (e): comparison of the input (solid red line) and extracted (dashed blue line) charge separation distributions for ions I^{2+}, I^{4+}, I^{5+} and I^{6+}, respectively.

Coulombic contribution to the KE of the ion is added, and the ion is recorded with a charge state of I^{n+}. If charge transfer does not occur, in the long distance/pump-probe limit, the signal is recorded as low KE (Channel II) $I^{(n+1)+}$. If charge transfer does not occur in the short distance/pump-probe limit, signal is not recorded (so as to be consistent with the experimental observation of a lack of pump-probe signals at the earliest time delays). Finally, the data were convoluted with the expected temporal and momentum resolution of the experiment.

Figure 18(a) shows the simulated Channel I signal for the I^{4+} ion, for a given input distribution of charge separations. Panels (b) to (e) compare the input charge separation distribution for iodine charge states I^{2+}, I^{4+}, I^{5+}, I^{6+} to that which is extracted from the simulated ion momentum data. This extraction was performed in the same manner as for the experimental data, assuming a constant dissociation velocity. In all cases, the agreement between the extracted and input distributions is very strong. As can be shown by further analysis, the slight differences observed are due to the finite experimental momentum resolution, which is a limiting factor of greater importance in the present experiments than the assumption of a single dissociation velocity.

Appendix I: Comparison of Channel I Analyzed in Delay and Momentum Domains

Figure 19 directly compares the analysis of Channel I in the delay and KER domains, corresponding to the analyses shown in Figs 2 and 3. Figure 19 highlights important physical differences between the information extracted in the two domains. The pump-probe delay encodes information about the geometry *at the point of ionization*, whereas the KER after Coulomb explosion relates to the geometry *at the point of charge transfer*. It can be seen that the charge transfer occurs at a narrow range of geometries relative to the distribution of geometries at the point of ionization. Furthermore, the center of the distribution of geometries at the point of ionization occurs at shorter distances than the distribution of geometries at the point of charge transfer. This implies that, when ionization occurs at shorter C-I distances (below 5 Å), charge transfer primarily occurs after some delay, during which the two fragments

continue to recoil from one another. This may be because the crossings between potential energy surfaces which mediate the charge transfer only occur at these more extended distances, as discussed below.

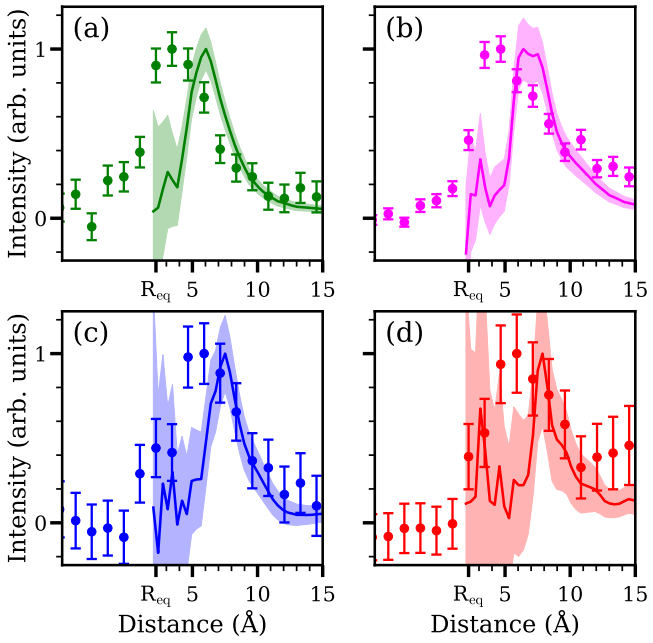

FIG. 19. Comparison of the analysis of high momentum ions in the pump-probe delay and momentum domains. The intensity of high momentum ions as a function of pump-probe delay, which has been converted to C-I distance at point of ionization, is shown as solid circular points. The charge separation distances, determined from the analysis of the ion momentum distributions, using the procedure described above, are shown as solid colored lines. The shaded region surrounding the solid lines are estimated error bars at the 1σ level.

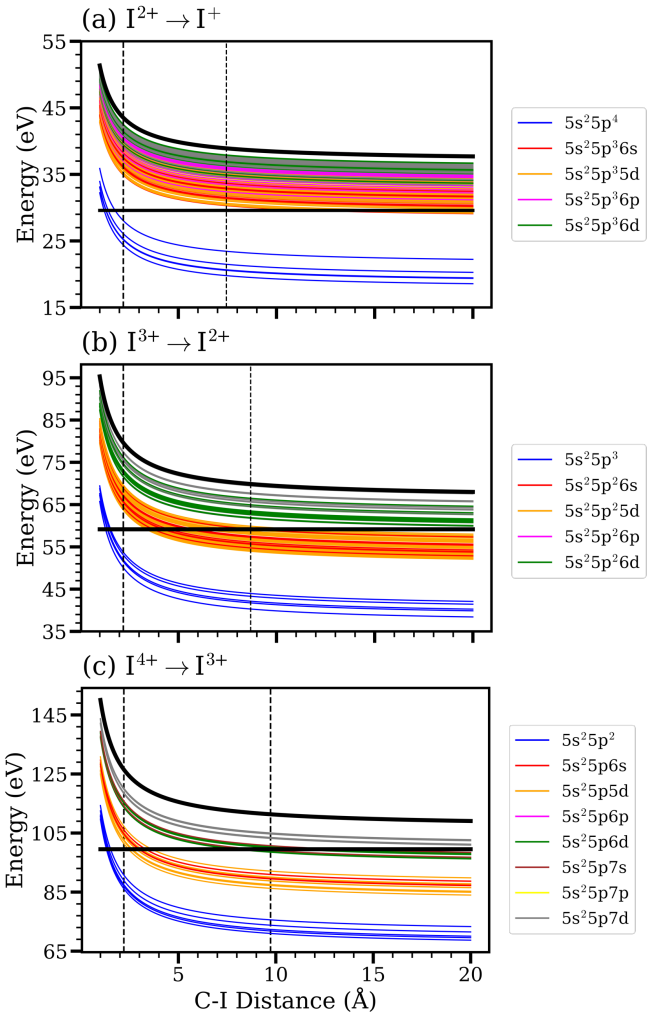

FIG. 20. Approximate potential energy curves relevant to the charge transfer processes: (a) $C_3H_7...I^{2+} \rightarrow C_3H_7^+...I^+$, (b) $C_3H_7...I^{3+} \rightarrow C_3H_7^+...I^{2+}$ and (c) $C_3H_7...I^{4+} \rightarrow C_3H_7^+...I^{3+}$. These are discussed in more detail in the text.

Appendix J: Electronic States Involved in Charge Transfer

For a given iodine charge state, $I^{(n+1)+}$, charge transfer (CT) should be expected to occur most efficiently at regions of strong coupling (i.e., near degeneracy) between potential energy surfaces of $(C_3H_7...I^{(n+1)+})$ and $(C_3H_7^+...I^{n+})$ character. To illustrate the concept, we here focus on approximate one-dimensional potential energy curves (PECs) along the C-I stretch coordinate, R_{C-I}. The energies of the ground states of the former at all but short R_{C-I} can be well-approximated by the sum of the ionization potentials leading to the $I^{(n+1)+}$ cation plus the bond dissociation energy $D_0(C_3H_7\text{-}I)$. Since $D_0(C_3H_7\text{-}I)$ is common to all channels it is henceforth neglected. The latter PECs are described by the energies of the different electronic states of the I^{n+} cation, along with the ionization potential of the ground state C_3H_7 radical and a Coulombic contribution. Figure 20 panels (a) to (c) show example illustrative PECs relevant for CT from I^{2+}, I^{3+} and I^{4+} to a ground state C_3H_7 partner. Ionization potentials and electronic energies were taken from the NIST atomic spectra database [54]. Only excited states of the I^{n+} cations which differ in electronic configuration by adding an electron into different unfilled orbitals of the ground state of the $I^{(n-1)+}$ cation are considered, and the states are color coded by their electronic configuration, as labelled. The energy of the $C_3H_7...I^{(n+1)+}$ ground electronic state is plotted as a bold, horizontal black line, whilst the convergence limit of the $C_3H_7...I^{n+}$ Rydberg series is also plotted as a bold black line. The equilibrium R_{C-I} bond distance in the ground state C_3H_7I molecule, as well as the critical distance for charge transfer from the classical over-the-barrier model, are indicated by dashed black vertical lines. Particularly in the case of Fig. 20(c), the apparent sparseness of $C_3H_7...I^{n+}$ PECs at higher energy

simply reflects the paucity of data listed in the NIST database. In actuality, the density of $C_3H_7...I^{n+}$ Rydberg curves will get ever higher upon approaching the series limit.

Any more complete picture will need to recognize the greater dimensionality of the problem and the approximations induced by neglecting any valence bonding contributions (which will be most serious for low n). Furthermore, whilst any $C_3H_7...I^{2+}$ to $C_3H_7^+...I^+$ CT might well show a propensity for forming intact ground state $C_3H_7^+$ fragments, the energy released during CT from higher $C_3H_7...I^{(n+1)+}$ systems may populate excited (dissociative) states of the propyl cation. The effects of such fragmentation can be approximately visualised within the framework of the 1D PECs shown in Fig. 20 by raising the manifold of any given set of $C_3H_7...I^{n+}$ curves by ∼4 eV per broken C-C or C-H bond.

[1] B. Erk, R. Boll, S. Trippel, D. Anielski, L. Foucar, B. Rudek, S. W. Epp, R. Coffee, S. Carron, S. Schorb, *et al.*, Science **345**, 288 (2014).
[2] T. Cravens, Geophys. Res. Lett. **24**, 105 (1997).
[3] T. Cravens, Science **296**, 1042 (2002).
[4] S. Snowden, M. Collier, and K. Kuntz, Astrophys. J. **610**, 1182 (2004).
[5] K. Dennerl, Space Sci. Rev. **157**, 57 (2010).
[6] S. D. Price, M. Manning, and S. R. Leone, J. Am. Chem. Soc. **116**, 8673 (1994).
[7] S. D. Price, Int. J. Mass. Spectrom. **260**, 1 (2007).
[8] S. D. Price, J. D. Fletcher, F. E. Gossan, and M. A. Parkes, Int. Rev. Phys. Chem. **36**, 145 (2017).
[9] R. A. Marcus and N. Sutin, Biochim. Biophys. Acta - Bioenerg. **811**, 265 (1985).
[10] A. M. Kuznetsov, *Charge transfer in physics, chemistry and biology: physical mechanisms of elementary processes and an introduction to the theory* (CRC Press, 2020).
[11] J. Feldhaus, J. Phys. B: At. Mol. Opt. Phys. **43**, 194002 (2010).
[12] P. Emma, R. Akre, J. Arthur, R. Bionta, C. Bostedt, J. Bozek, A. Brachmann, P. Bucksbaum, R. Coffee, F.-J. Decker, *et al.*, Nat. Photonics **4**, 641 (2010).
[13] T. Ishikawa, H. Aoyagi, T. Asaka, Y. Asano, N. Azumi, T. Bizen, H. Ego, K. Fukami, T. Fukui, Y. Furukawa, *et al.*, Nat. Photonics **6**, 540 (2012).
[14] H. Fukuzawa, S.-K. Son, K. Motomura, S. Mondal, K. Nagaya, S. Wada, X.-J. Liu, R. Feifel, T. Tachibana, Y. Ito, *et al.*, Phys. Rev. Lett. **110**, 173005 (2013).
[15] B. Erk, D. Rolles, L. Foucar, B. Rudek, S. W. Epp, M. Cryle, C. Bostedt, S. Schorb, J. Bozek, A. Rouzee, *et al.*, Phys. Rev. Lett. **110**, 053003 (2013).
[16] F. Braußе, G. Goldsztejn, K. Amini, R. Boll, S. Bari, C. Bomme, M. Brouard, M. Burt, B. C. De Miranda, S. Düsterer, *et al.*, Phys. Rev. A **97**, 043429 (2018).
[17] M. Ilchen, P. Schmidt, N. M. Novikovskiy, G. Hartmann, P. Rupprecht, R. N. Coffee, A. Ehresmann, A. Galler, N. Hartmann, W. Helml, *et al.*, Commun. Chem. **4**, 1 (2021).
[18] F. Allum, N. Anders, M. Brouard, P. Bucksbaum, M. Burt, B. Downes-Ward, S. Grundmann, J. Harries, Y. Ishimura, H. Iwayama, *et al.*, Faraday Discuss. **228**, 571 (2021).
[19] H. Ryufuku, K. Sasaki, and T. Watanabe, Phys. Rev. A **21**, 745 (1980).
[20] A. Niehaus, J. Phys. B: At. Mol. Opt. Phys. **19**, 2925 (1986).
[21] R. Boll, B. Erk, R. Coffee, S. Trippel, T. Kierspel, C. Bomme, J. D. Bozek, M. Burkett, S. Carron, K. R. Ferguson, *et al.*, Struct. Dyn. **3**, 043207 (2016).
[22] K. Amini, E. Savelyev, F. Braußе, N. Berrah, C. Bomme, M. Brouard, M. Burt, L. Christensen, S. Düsterer, B. Erk, *et al.*, Struct. Dyn. **5**, 014301 (2018).
[23] R. Forbes, F. Allum, S. Bari, R. Boll, K. Borne, M. Brouard, P. H. Bucksbaum, N. Ekanayake, B. Erk, A. J. Howard, *et al.*, J. Phys. B: At. Mol. Opt. Phys. **53**, 224001 (2020).
[24] H. Köckert, J. Lee, F. Allum, K. Amini, S. Bari, C. Bomme, F. Braußе, M. Brouard, M. Burt, B. C. de Miranda, *et al.*, J. Phys. B: At. Mol. Opt. Phys. (2022).
[25] S. Owada, K. Togawa, T. Inagaki, T. Hara, T. Tanaka, Y. Joti, T. Koyama, K. Nakajima, H. Ohashi, Y. Senba, T. Togashi, K. Tono, M. Yamaga, H. Yumoto, M. Yabashi, H. Tanaka, and T. Ishikawa, J. Synchrotron Radiat. **25**, 282 (2018).
[26] M. E. Corrales, V. Loriot, G. Balerdi, J. González-Vázquez, R. de Nalda, L. Banares, and A. H. Zewail, Phys. Chem. Chem. Phys. **16**, 8812 (2014).
[27] M. A. Todt, S. Datta, A. Rose, K. Leung, and H. F. Davis, Phys. Chem. Chem. Phys. **22**, 27338 (2020).
[28] N. Saito and I. H. Suzuki, Int. J. Mass Spectrom. Ion Process. **115**, 157 (1992).
[29] J. W. Au, G. Cooper, G. R. Burton, T. N. Olney, and C. Brion, Chem. Phys. **173**, 209 (1993).
[30] A. T. J. B. Eppink and D. H. Parker, Rev. Sci. Instrum. **68**, 3477 (1997),.
[31] H. Fukuzawa, K. Nagaya, and K. Ueda, Nucl. Instrum. Methods Phys. Res. A: Accel. Spectrom. Detect. Assoc. Equip. **907**, 116 (2018),.
[32] S. Owada, K. Nakajima, T. Togashi, T. Katayama, H. Yumoto, H. Ohashi, and M. Yabashi, J. Synchrotron Radiat. **26**, 887 (2019).
[33] H. Stapelfeldt, E. Constant, and P. Corkum, Phys. Rev. Lett. **74**, 3780 (1995).
[34] F. Allum, M. Burt, K. Amini, R. Boll, H. Köckert, P. K. Olshin, S. Bari, C. Bomme, F. Braußе, B. Cunha de Miranda, *et al.*, J. Chem. Phys. **149**, 204313 (2018).
[35] J. W. McManus, T. Walmsley, K. Nagaya, J. R. Harries, Y. Kumagai, H. Iwayama, M. N. Ashfold, M. Britton, P. H. Bucksbaum, B. Downes-Ward, *et al.*, Phys. Chem. Chem. Phys. **24**, 22699 (2022).
[36] F. Allum, V. Music, L. Inhester, R. Boll, B. Erk, P. Schmidt, T. M. Baumann, G. Brenner, M. Burt, P. V. Demekhin, *et al.*, Commun. Chem. **5**, 1 (2022).
[37] C. Ellert, H. Stapelfeldt, E. Constant, H. Sakai, J. Wright, D. Rayner, and P. Corkum, Philos. Trans. Royal Soc. A **356**, 329 (1998).
[38] J. S. Wright, G. DiLabio, D. Matusek, P. Corkum, M. Y. Ivanov, C. Ellert, R. Buenker, A. Alekseyev, and

G. Hirsch, Phys. Rev. A **59**, 4512 (1999).
[39] F. Penent, P. Lablanquie, J. Palaudoux, L. Andric, G. Gamblin, Y. Hikosaka, K. Ito, and S. Carniato, Phys. Rev. Lett. **106**, 103002 (2011).
[40] M. E. Corrales, G. Gitzinger, J. González-Vázquez, V. Loriot, R. de Nalda, and L. Banares, J. Phys. Chem. A **116**, 2669 (2012).
[41] S. W. Crane, L. Ge, G. A. Cooper, B. P. Carwithen, M. Bain, J. A. Smith, C. S. Hansen, and M. N. Ashfold, J. Phys. Chem. A **125**, 9594 (2021).
[42] R. Mann, F. Folkmann, and H. Beyer, J. Phys. B: At. Mol. Opt. Phys. **14**, 1161 (1981).
[43] H. Ryufuku and T. Watanabe, Phys. Rev. A **18**, 2005 (1978).
[44] P. Beiersdorfer, R. Olson, G. Brown, H. Chen, C. Harris, P. Neill, L. Schweikhard, S. Utter, and K. Widmann, Phys. Rev. Lett. **85**, 5090 (2000).
[45] J. Greenwood, I. Williams, S. Smith, and A. Chutjian, Phys. Rev. A **63**, 062707 (2001).
[46] S. Bliman, R. Bruch, M. Cornille, A. Langereis, and J. Nordgren, Phys. Rev. A **66**, 052707 (2002).
[47] P. Beiersdorfer, K. Boyce, G. Brown, H. Chen, S. Kahn, R. Kelley, M. May, R. Olson, F. Porter, C. Stahle, *et al.*, Science **300**, 1558 (2003).
[48] S. Otranto, R. E. Olson, and P. Beiersdorfer, Phys. Rev. A **73**, 022723 (2006).
[49] F. Allum, C. Cheng, A. J. Howard, P. H. Bucksbaum, M. Brouard, T. Weinacht, and R. Forbes, J. Phys. Chem. Lett. **12**, 8302 (2021).
[50] D. Matsakis, A. Coster, B. Laster, and R. Sime, Phys. Today **72**, 10 (2019), and references therein.
[51] S. Owada, M. Fushitani, A. Matsuda, H. Fujise, Y. Sasaki, Y. Hikosaka, A. Hishikawa, and M. Yabashi, Characterization of soft X-ray FEL pulse duration with two-color photoelectron spectroscopy, J. Synchrotron Radiat. **27**, 1362 (2020).
[52] T. Tanaka, M. Kato, N. Saito, S. Owada, K. Tono, M. Yabashi, and T. Ishikawa, Absolute laser-intensity measurement and online monitor calibration using a calorimeter at a soft x-ray free-electron laser beamline in sacla, Nucl. Instrum. Methods Phys. Res. A: Accel. Spectrom. Detect. Assoc. Equip. **894**, 107 (2018).
[53] V. A. Shubert, M. Rednic, and S. T. Pratt, Photodissociation of i-C_3H_7I within the A band and anisotropy-based decomposition of the translational energy distributions, J. Chem. Phys **130**, 134306 (2009).
[54] A. Kramida, Yu. Ralchenko, J. Reader, and and NIST ASD Team, NIST Atomic Spectra Database (ver. 5.9), [Online]. Available: `https://physics.nist.gov/asd` [2022, June 5]. National Institute of Standards and Technology, Gaithersburg, MD. (2021).
[55] J. Dyke, A. Ellis, N. Jonathan, and A. Morris, Vacuum ultraviolet photoelectron spectroscopy of transient species. part 18.—the cyclopropyl, isopropyl and n-propyl radicals, J. Chem. Soc., Faraday Trans. 2, **81**, 1573 (1985).